Check for updates

Lanthanide/actinide boride nanoclusters and nanomaterials based on boron frameworks consisting of conjoined B_n rings (n = 7–9)†

Xiao-Qin Lu,[ab] Xiao-Ni Zhao,[a] Yue-Wen Mu [ID] *[a] and Si-Dian Li [ID] *[a]

Extensive global minimum searches augmented with first-principles theory calculations performed in this work indicate that the experimentally observed perfect inverse sandwich lanthanide boride complexes D_{7h} La$_2$B$_7^-$ (**1**), D_{8h} La$_2$B$_8$ (**3**), D_{9h} La$_2$B$_9^-$ (**7**) can be extended to their actinide counterparts C_{2v} Ac$_2$B$_7^-$ (**1'**), D_{8h} Ac$_2$B$_8$ (**3'**), D_{9h} Ac$_2$B$_9^-$ (**7'**) with a B_n monocyclic ring (n = 7–9) sandwiched by two Ac dopants. Such M$_2$B$_n^{-/0}$ inverse sandwiches (**1/1'**, **3/3'**, **7/7'**) can be used as building blocks to generate the ground-state C_2 La$_4$B$_{13}^-$ (**2**)/Ac$_4$B$_{13}^-$ (**2'**), D_2 La$_4$B$_{15}^-$ (**4**)/Ac$_4$B$_{15}^-$ (**4'**), C_{3v}/C_3 La$_4$B$_{18}$ (**5**)/Ac$_4$B$_{18}$ (**5'**), O_h Ac$_7$B$_{24}^+$ (**6'**), O_h Ac$_7$B$_{24}$, T_d Ac$_4$B$_{24}$ (**8'**), C_1 La$_5$B$_{24}^+$ (**9**)/Ac$_5$B$_{24}^+$ (**9'**), and T_d Ac$_4$B$_{29}^-$ (**10'**) which are based on boron frameworks consisting of multiple conjoined B_n rings (n = 7–9). Detailed bonding analyses show that effective (d−p)σ, (d−p)π and (d−p)δ coordination bonds are formed between the B_n rings and metal doping centers, conferring three-dimensional aromaticity and extra stability to the systems. In particular, the perfect body-centered cubic O_h Ac$_7$B$_{24}^+$ (**6'**) and O_h Ac$_7$B$_{24}$ with six conjoined B_8 rings can be extended in x, y, and z dimensions to form one-dimensional Ac$_{10}$B$_{32}$ (**11'**), two-dimensional Ac$_3$B$_{10}$ (**12'**), and three-dimensional AcB$_6$ (**13'**) nanomaterials, presenting a B_8-based bottom-up approach from metal boride nanoclusters to their low-dimensional nanomaterials.

Introduction

As the light neighbour of carbon in the periodic table with prototypical electron-deficiency, boron exhibits unique structures and bonding in its polyhedral molecules, bulk allotropes,[1] and the theoretically predicted buckyballs[2] and newly observed bilayer borophenes.[3] In the past two decades, persistent joint photoelectron spectroscopy (PES) and first-principles theory investigations have revealed that small boron clusters B_n^- possess planar or quasi-planar (n = 3–38, 41, and 42), cage-like ($B_{40}^{-/0}$/B_{39}^-), and bilayer ($B_{48}^{-/0}$) structures in a wide size range between n = 3–48, featuring both delocalized σ and π multicenter-two-electron (mc-2e) bonding interactions.[4–9] Combined ion-mobility measurements and density functional theory (DFT) investigations indicated that cationic boron clusters B_n^+ possess double-ring tubular structures (n = 16–25).[10] The experimentally observed cage-like $B_{40}^{-/0}$/B_{39}^- have been extended to the B_n^q borospherene family (n = 36–42, q = n − 40)

at first-principles theory level, while the bilayer structural motif firstly observed in $B_{48}^{-/0}$ has been expanded recently to a series of novel bilayer boron clusters in the size range between B_{50}–B_{72} and a bottom-up approach from medium-sized boron clusters to bilayer borophenes at DFT level.[11] In addition, icosahedral-B_{12} stuffed B_{80}, B_{84}, B_{102}, and B_{112} have been predicted at DFT level, with C_s B_{112} as the most stable core–shell borospherene with one B_{12} icosahral core at the center reported to date.[12–15] The structures of small and, especially, medium-sized boron clusters appear to exhibit strong dependence on both their sizes and charge states.

Transition-metal-doping has proven to induce dramatic structural changes to boron clusters, greatly enriching the structural diversity of metal boride complexes. Mono-metal-doped boron clusters exhibit metal-centered planar wheel-like, half-sandwich, or tubular drum-like structures, generating the coordination number of CN = 10 in planar D_{10h} Ta©B$_{10}^-$ and D_{10h} Nb©B$_{10}^-$.[16–21] A recent investigation indicates that the experimentally observed perfect planar D_{13h} La©C$_{13}^+$ possesses the record coordination number of CN = 13 in planar species.[22] A series of perfect inverse-sandwich di-metal-doped boron clusters D_{6h} Ta$_2$B$_6^{-/0}$, D_{7h} La$_2$B$_7^-$ (**1**), D_{8h} La$_2$B$_8$ (**3**), and D_{9h} La$_2$B$_9^-$ (**7**) were recently discovered in PES measurements, with a perfect planar B_n ring (n = 6–9) sandwiched between two metal atoms *via* effective (d−p)σ, (d−p)π, and (d−p)δ coordination

[a] Nanocluster Laboratory, Institute of Molecular Science, Shanxi University, Taiyuan 030006, China. E-mail: ywmu@sxu.edu.cn, lisidian@sxu.edu.cn

[b] Shanxi Center for Testing of Functional Agro-Products, Shanxi Agricultural University, Taiyuan 030031, China

† Electronic supplementary information (ESI) available. See DOI: https://doi.org/10.1039/d2cp03142f

bonding interactions.[23–25] However, both C_1 $La_2B_{10}^-$ and C_{2v} $La_2B_{11}^-$ were experimentally characterized to be expanded inverse sandwiches based on a B_8 ring, indicating that the B_9 is the largest boron ring to form perfect inverse-sandwich metal boride complexes.[26] The tri-La-doped inverse triple-decker C_{2v} $La_3B_{14}^-$ was discovered in PES experiments with two conjoined B_8 rings sharing a B–B edge.[27] PES experiments indicate $La_3B_{18}^-$ is a perfect D_{3h} trihedral metallo-borospherene with three deca-coordinate La atoms on the cage surface.[28] Such a metallo-borospherene was late theoretically extended to the smallest core–shell metallo-borospherene D_{3h} $La_3B_{20}^-$ ($B_2@La_3B_{18}^-$) with a B_2 dumb-bell at the cage center along the C_3 molecular axis.[29] Based on extensive global minimum (GM) searches and first-principles theory calculations, our group recently proposed a series of novel lanthanide boride nanoclusters including the smallest double-ring tubular molecular rotor C_{2h} $La_2[B_2@B_{18}]$ with a B_2 dumb-bell inside,[30] perfect endohedral cubic O_h $La_7B_{24}^+$ (**6**) and O_h La_7B_{24} with six conjoined inverse La_2B_8 sandwiches sharing a La atom at the center, perfect tetrahedral metallo-borospherene T_d La_4B_{24} (**8**) with four nona-coordinate La atoms on the cage surface, perfect tetrahedral core–shell metallo-borospherene T_d $La_4B_{29}^{0/+/-}$ (**10**) ($B@B_4@La_4B_{24}$) with a tetrahedral BB_4 unit at the center, and endohedral trihedral metallo-borospherenes D_{3h} $La@[La_5\&B_{30}]^{0/2-}$ with spherical aromaticity.[31–33] However, tetra-La-doped boride complexes $La_4B_n^{-/0}$ (n = 13–18) with conjoined B_7, B_8, and B_9 rings as ligands still remain unknown in both experiments and theory, and more importantly, the chemistry and materials science of the corresponding actinide boride nanoclusters and their low-dimensional nanomaterials have not been explored to date in either experiments or theory possibly due to the radioactivity of actinide. Modern quantum chemistry provides powerful means to fulfil the gaps in such situations.

Inspired by the experimentally observed perfect inverse sandwich $La_2B_7^-$ (**1**), La_2B_8 (**3**), $La_2B_9^-$ (**7**) and based on extensive first-principles theory calculations, we predict herein a series of novel La/Ac doped boron clusters including C_{2v} $Ac_2B_7^-$ (**1′**), D_{8h} Ac_2B_8 (**3′**), D_{9h} $Ac_2B_9^-$ (**7′**), C_2 $La_4B_{13}^-$ (**2**)/$Ac_4B_{13}^-$ (**2′**), D_2 $La_4B_{15}^-$ (**4**)/$Ac_4B_{15}^-$ (**4′**), C_{3v}/C_3 La_4B_{18} (**5**)/Ac_4B_{18} (**5′**), O_h $Ac_7B_{24}^+$ (**6′**), T_d Ac_4B_{24} (**8′**), C_1 $La_5B_{24}^+$ (**9**)/$Ac_5B_{24}^+$ (**9′**), and T_d $Ac_4B_{29}^-$ (**10′**) which are composed of mono or multiple conjoined B_n rings (n = 7–9) as ligands to coordinate the metal centres. More interestingly, the cubic $Ac_7B_{24}^{+/0}$ (**6′**) can be extended to form the highly stable actinide boride nanomaterials 1D $Ac_{10}B_{32}$ (**11′**), 2D Ac_3B_{10} (**12′**), and 3D AcB_6 (**13′**), expanding the previously reported low-dimensional lanthanide boride nanomaterials to their actinide boride counterparts.

Theoretical methods

The global-minimum (GM) structures of $La_4B_{13}^-$, $La_4B_{15}^-$, La_4B_{18}, and $La_5B_{24}^+$ were searched using the TGMin2 program[34] at the DFT level, with the initial seeds constructed based on the experimentally observed La–B binary complexes. More than 3000 trial structures were explored for each species at PBE/TZVP. The low-lying isomers were subsequently optimized using the hybrid PBE0[35] and TPSSh[36] functional with the 6-311+G* basis set[37] for B and Stuttgart energy-consistent relativistic pseudopotential ECP46MWB[38,39] and ECP78MWB[40] for La and Ac using the Gaussian 09 program.[41] All local minima were checked by vibrational frequency analyses. To obtain more accurate relative energies, we did further single-point CCSD(T) calculations[42–44] at the PBE0 geometries with the same basis sets for the five lowest-lying isomers of $La_4B_{13}^-$, $La_4B_{15}^-$, and La_4B_{18} using the Molpro package.[45] Based on the obtained low-lying isomers of $La_2B_7^-$, $La_4B_{13}^-$, La_2B_8, $La_4B_{15}^-$, La_4B_{18}, $La_7B_{24}^+$, $La_2B_9^-$, La_4B_{24}, $La_5B_{24}^+$, and $La_4B_{29}^-$, we optimized the structures of their actinide boride counterparts $Ac_2B_7^-$, $Ac_4B_{13}^-$, Ac_2B_8, $Ac_4B_{15}^-$, Ac_4B_{18}, $Ac_7B_{24}^+$, $Ac_2B_9^-$, Ac_4B_{24}, $Ac_5B_{24}^+$, and $Ac_4B_{29}^-$. Low dimensional actinide boride nanostructures 1D $Ac_{10}B_{32}$, 2D Ac_3B_{10}, and 3D AcB_6 constructed from cubic $Ac_7B_{24}^+$ (**6′**) were fully optimized using the Vienna *ab initio* simulation package (VASP),[46,47] within the framework of projector augmented wave (PAW)[48,49] pseudopotential method and PBE generalized gradient approximation (GGA).[50] The Coulomb-corrected local spin-density approximation (LSDA + U) was utilized for both structural relaxation and static calculation (U = 5 eV) for La and Ac.[51,52] Different long-range corrections with U = 3, 4, and 5 are found to produce essentially the same lattice constants and band structures for low-dimensional actinide materials. The cutoff energy of 500 eV was used. The criterion of convergence for the maximum force on each atom was less than 0.01 eV Å^{-1} and the total energy was 10^{-5} eV. Chemical bonding was analyzed using the adaptive natural density partitioning (AdNDP) approach.[53] Natural bonding orbital (NBO) analyses were performed using the NBO 6.0 program.[54] Born–Oppenheimer molecular dynamics (BOMD) simulations were carried out on $La_4B_{13}^-$ (**2**), $La_4B_{15}^-$ (**4**), and La_4B_{18} (**5**) for 30 ps at 800 K using the CP2K code.[55] The iso-chemical shielding surfaces (ICSSs)[56] were generated with the Multiwfn 3.8 code.[57]

Results and discussion

Lanthanide/actinide boride nanoclusters consisting of conjoined B_n rings (n = 7–9)

As elements in the same group in the periodic table, Ac([Rn]$7s^2 6d^1$) and La([Xe]$6s^2 5d^1$) with similar valence electronic configuraitons are expected to form similar boroide nanoclusters and nanomaterials. It turned out to be true that, by substitution of La with Ac, the experimentally observed inverse sandwich lanthanide boride clusters D_{7h} $La_2B_7^{-/0}$ (**1**, $^3A_2'$), D_{8h} La_2B_8 (**3**, $^3A_{2g}$), D_{9h} $La_2B_9^-$ (**7**, $^1A_1'$) can be readily extended to their actinide counterparts D_{7h} $Ac_2B_7^-$ ($^3A_2'$), D_{8h} Ac_2B_8 (**3′**, $^3A_{2g}$), and D_{9h} $Ac_2B_9^-$ (**7′**, $^1A_1'$) at PBE0, with the average optimized B–B, Ac–B, and Ac–Ac distances of r_{B-B} = 1.587, 1.554, and 1.542 Å, r_{Ac-B} = 2.705, 2.807, and 2.890 Å, and r_{Ac-Ac} = 3.987, 3.878, and 3.617 Å, respectively. However, at the more accurate CCSD(T) level, the triplet D_{7h} $Ac_2B_7^-$ is slightly

This journal is © the Owner Societies 2022

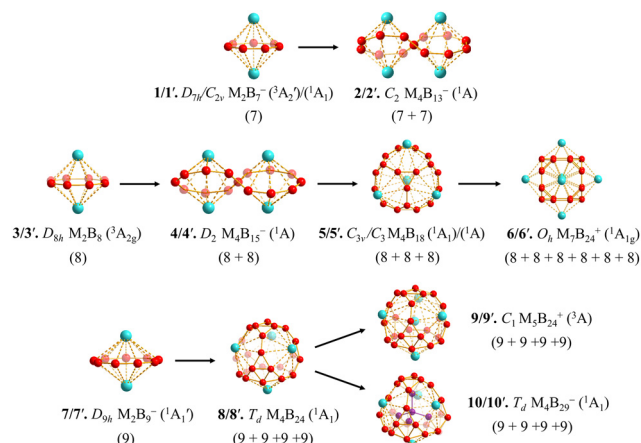*Phys. Chem. Chem. Phys.*, 2022, **24**, 21078–21084 | **21079**

Fig. 1 Lanthanide and actinide boride nanoclusters consisting of mono or multiple conjoined B_n rings (n = 7–9) (M = La, Ac). The number of B_n rings (n = 7–9) in each structure is indicated in parentheses.

distorted to singlet C_{2v} $Ac_2B_7^-$ ($\mathbf{1'}$, $^1A_1$) which appears to be 0.56 eV more stable than its D_{7h} counterpart (Fig. S1(a), ESI†). $Ac_2B_n^{-/0}$ ($\mathbf{1'}$, $\mathbf{3'}$, $\mathbf{7'}$) as the global minima of the systems appear to lie at least 0.56 eV lower than their counterparts in other structural motifs at CCSD(T) (Fig. S1–S3, ESI†).

Using inverse sandwich $M_2B_7^-$ ($\mathbf{1/1'}$) as building blocks, the axially chiral C_2 $M_4B_{13}^-$ ($\mathbf{2/2'}$) based on a B_{13} boron framework consisting of two conjoined B_7 rings sharing a periphery B atom at the center in a ∞-shaped structural motif (7 + 7 mode) were obtained. Interestingly and encouragingly, as shown in Fig. 1 and Fig. S1($\mathbf{2}$) (ESI†), extensive GM searches and first-principles calculations indicate that C_2 $La_4B_{13}^-$ ($\mathbf{2}$, ^1A) composed of two conjoined $La_2B_7^-$ ($\mathbf{1}$) inverse sandwiches is the well-defined GM of the system with the lowest vibrational frequency of v_{min} = 79.3 cm^{-1} which lies 0.82 eV lower in energy than its triplet counterpart D_2 $La_4B_{13}^-$ ($^3B_2$) at CCSD(T), with all other low-lying isomers lying at least 0.41 eV higher in relative energy. In addition to the shared B atom, $La_4B_{13}^-$ ($\mathbf{2}$) also forms two vertex-sharing B_3 triangles involving the central B and its four closest periphery boron neighbors as bridges to link the two equivalent B_7 rings together, faciliating the formation of multiple-center bonding interactions over the two vertex-sharing B_3 triangles to help stabilize the system as detailed below. As shown in Fig. S4 (ESI†), $La_4B_{13}^-$ ($\mathbf{2}$) possesses the optimized B–B distance of r_{B-B} = 1.75 Å between central B and its four closest neighbors which is longer than the average B–B distance of r_{B-B} = 1.62 Å in the remaining parts of the two conjoined B_7 rings, while the La–B distances of r_{La-B} = 2.63 Å between the central B and four La atoms appear to be shorter than the remaining La–B distances with r_{La-B} = 2.68–2.71 Å. Detailed NBO analyses on $La_4B_{13}^-$ ($\mathbf{2}$) show that central B atom possesses the natural atomic charge of q_B = −0.63 |e| and total Wiberg bond order of WBI_B = 3.92, while the four equivalent La atoms carry the natural atomic charge of q_{La} = +1.10 |e| and total Wiberg bond order of WBI_{La} = 3.27. The B–B bond order between central B and its four neighboring B is calculated to be WBI_{B-B} = 0.60. Molecular dynamics simulations in 30 ps

indicate that $La_4B_{13}^-$ ($\mathbf{2}$) is highly dynamically stable, with the small calculated average root-mean-square-deviations of RMSD = 0.13 Å and maximum bond length deviations of MAXD = 0.37 Å at 800 K (Fig. S5a, ESI†). Similar to $La_4B_{13}^-$ ($\mathbf{2}$), C_2 $Ac_4B_{13}^-$ ($\mathbf{2'}$, ^1A) also proves to be the GM of the system (Fig. S1($\mathbf{2'}$) (ESI†)) dynamically table at 800 K. (Fig. S5b, ESI†).

Employing M_2B_8 ($\mathbf{3/3'}$) as building blocks, we obtained the axially chiral singlet D_2 $M_4B_{15}^-$ ($\mathbf{4/4'}$) which possesses two conjoined equivalent B_8 rings in a ∞-shaped structural motif (8 + 8 mode), with two vertex-sharing B_3 triangles formed between the B atom at the center and its four closest boron neighbors, similar to the situation in $M_4B_{13}^-$ ($\mathbf{2/2'}$). D_2 $La_4B_{15}^-$ ($\mathbf{4}$) proves to be the well-defined GM of the system (Fig. S2, ESI†) with the lowest vibrational frequency of v_{min} = 65.5 cm^{-1} at PBE0 which lies 0.75 and 0.79 eV lower at CCSD(T) than the second (C_1) and third (C_s) lowest-lying isomers, respectively. It possesses the optimized B–B distance of r_{B-B} = 1.73 Å between central B and its four closest B neighbours and La–B distance of r_{La-B} = 2.68 Å between central B and four La atoms. The calculated HOMO–LUMO gap of ΔE_{gap} = 1.96 eV at PBE0 well supports the high chemical stability of the monoanionic complex. Its four equivalent La atoms possess the natural atomic charge of q_{La} = +1.18 |e|, the electronic configuration of La[Xe]5d$^{1.60}$6s$^{0.14}$, and the total Wiberg bond order of WBI_{La} = 3.14. The La–B coordination bond order between La and central B is calculated to be WBI_{La-B} = 0.26 which is slightly lower than the other La–B bond orders between La and its neighboring B_8 ring. Extensive molecular dynamics simulations indicate that $La_4B_{15}^-$ ($\mathbf{4}$) is also highly dynamically stable at 800 K (Fig. S5a, ESI†). As the actinide analogue of $La_4B_{15}^-$ ($\mathbf{4}$), D_2 $Ac_4B_{15}^-$ ($\mathbf{4'}$) also appears to be highly stable both thermo-dynamically and dynamically (Fig. S5b, ESI†). However, extensive global searches indicate that, unlike B_7 and B_8 rings, B_9 rings are too big in size to form stable conjoined double-ring metal complexes.

We further extend the complex series to the crown-like C_{3v} M_4B_{18} ($\mathbf{5/5'}$) which consist of three conjoined B_8 rings sharing a B_3 triangle on the top, with three equivalent octa-coordinate La atoms on the cage surface and one La atom inside at the center along the C_3 molecular axis. Extensive GM searches indicate that La_4B_{18} ($\mathbf{5}$) is the GM of the system at CCSD(T), with the second lowest-lying cage-like C_s isomer lying 0.07 eV higher in relative energy. Other cage-like isomers are found to be at least 0.81 eV less stable than the GM (Fig. S2($\mathbf{5}$), ESI†). La_4B_{18} ($\mathbf{5}$) possesses the optimized average La–B distances of r_{La-B} = 2.89 Å between the central La atom and its B_{18} ligand and r_{La-B} = 2.72 Å between the octa-coordinate La atoms and their neighboring B_8 ligands on the surface, with the B–B distances of r_{B-B} = 1.69 Å within the three B–B dumb-bells shared by neighboring B_8 rings and r_{B-B} = 1.63 Å within the B_3 triangles on the top. The large HOMO–LUMO gap of ΔE_{gap} = 2.37 eV calculated for La_4B_{18} ($\mathbf{5}$) well supports the high chemical stability of the system with three conjoined B_8 rings. Similar situation exists in C_{3v} Ac_4B_{18} ($\mathbf{5'}$). In contrast, extensive efforts to construct boron frameworks with three conjoined B_7 or B_9 rings have proven to be unsuccessful. Furthermore, using the

B_8-based bottom-up approach established above from M_2B_8 (3/3′), $M_4B_{15}^-$ (4/4′), and M_4B_{18} (5/5′), the crown-shaped La_4B_{18} (5) with dangling bonds at the bottom can be further expanded to form boron frameworks with more than three conjoined B_8 rings based on the special topology of the B_8 ring. The perfect cubic O_h $M_7B_{24}^+$ (6/6′) with six conjoined B_8 rings provide such special cases which can be viewed as two conjoining M_4B_{18} (5/5′) units along the C_3 molecular axis.

Further increasing the cluster sizes, our group reported in two recent papers on singlet O_h $La_7B_{24}^+$ (6) and doublet O_h La_7B_{24} with six conjoined B_8 rings, tetrahedral T_d La_4B_{24} (8) with four conjoined B_9 rings, and tetrahedral T_d $La_4B_{29}^-$ (10) with four conjoined B_9 rings encapsulating a tetrahedral BB_4 core at the center.[31,32] We focus here on their actinide analogues O_h $Ac_7B_{24}^+$ (6′), O_h Ac_7B_{24}, T_d Ac_4B_{24} (8′), T_d $Ac_4B_{29}^-$ (10′), and the newly obtained core–shell C_1 $M_5B_{24}^+$ (9/9′) (M = La, Ac). Both the endohedral singlet $Ac_7B_{24}^+$ (6′) and doublet O_h Ac_7B_{24} which can be viewed as six embedded La_2B_8 inverse sandwiches in a cube sharing a La vertex at the center possess perfect body-centered structures with six equivalent octa-coordinate Ac atoms on the surface and one Ac atom at the center, T_d Ac_4B_{24} (8′) as an ideal tetrahedral metallo-borosphere contains a boron framework consisting of four conjoined B_9 rings with four equivalent nona-coordinate Ac atoms as integrated parts of the cage surface, C_1 $La_5B_{24}^+$ (9) and C_1 $Ac_5B_{24}^+$ (9′) are slightly distorted endohedral tetrahedral metallo-borospherenes with four nona-coordinate metal atoms on the surface and one metal atom slightly off-centered, while T_d $Ac_4B_{29}^-$ (10′) has a perfect tetrahedral core–shell structure with a tetrahedral T_d BB_4 unit encapsulated at the center. The low-lying isomers of the concerned species collectively depicted in Fig. S1–S3 (ESI†) indicate that lanthanide and actinide boride nanoclusters possess similar GMs and low-lying isomers in this size range.

Chemical bonding analyses

To better comprehend the high stability of La/Ac boride complexes with multiple conjoined B_n rings (n = 7–9), as examples, we performed detailed AdNDP bonding analyses on the closed-shell C_2 $La_4B_{13}^-$ (2), D_2 $La_4B_{15}^-$ (4), and C_{3v} La_4B_{18} (5) to recover both the localized and delocalized bonds of the systems. As clearly indicated in Fig. 2a, $La_4B_{13}^-$ (2) possesses in the first row 5 2c-2e B–B periphery σ bonds on each of the two conjoined B_7 rings with the occupation number of ON = 1.87–1.89 |e| and 2 equivalent 3c-2e σ bonds on the two vertex-sharing B_3 triangles at the center with ON = 1.82 |e|, forming the σ-skeleton of the complex in an overall symmetry of C_2. The second row contains 3 9c-2e $B_7(\sigma)$–$La_2(d_{\pi/\sigma})$ bonds over the $La_2B_7^-$ inverse sandwich on the left with ON = 1.90–2.00 |e| and 3 symmetrically distributed 9c-2e $B_7(\sigma)$–$La_2(d_{\pi/\sigma})$ bonds over the $La_2B_7^-$ inverse sandwich on the right, forming two equivalent local σ aromatic inverse sandwiches matching the $4n + 2$ rule (n = 1) in $La_4B_{13}^-$ (2). The two conjoined locally σ-aromatic systems in $La_4B_{13}^-$ (2) well correspond to the σ aromatic system in the experimentally observed inverse sandwich D_{7h} $La_2B_7^-$ (1).[24] The 5c-2e π bond with ON = 1.67 in the third row and four 9c-2e $B_7(\pi)$–$La_2(d_{\pi/\sigma})$ bonds with ON = 1.98–1.99 |e| at
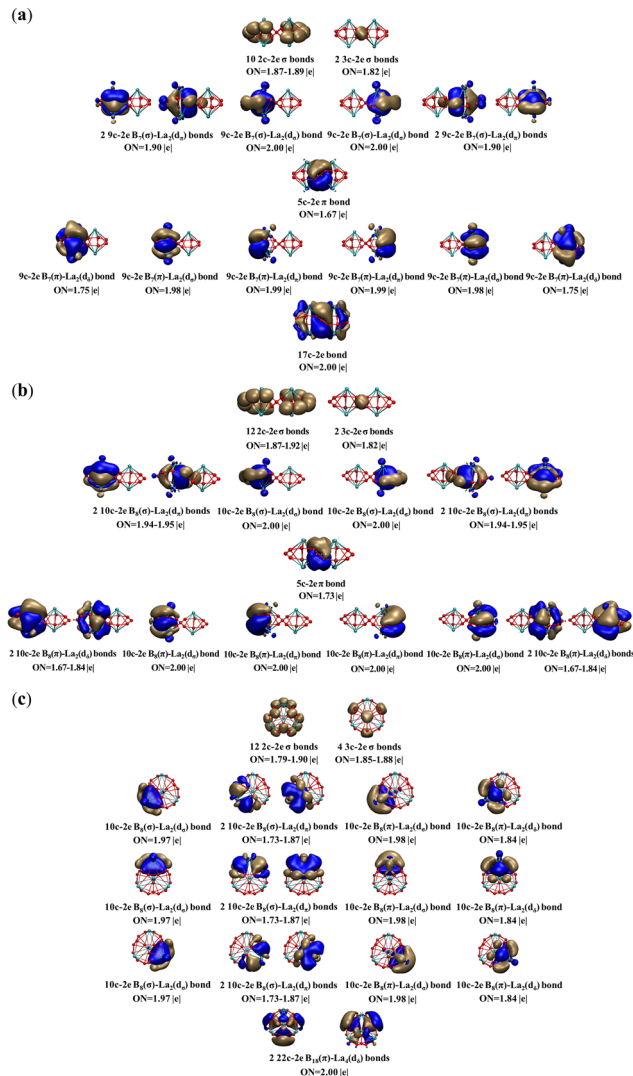
Fig. 2 AdNDP bonding patterns of the closed-shell (a) C_2 $La_4B_{13}^-$ (2), (b) D_2 $La_4B_{15}^-$ (4), and (c) C_{3v} La_4B_{18} (5), with the occupation numbers (ONs) indicated.

the center in the fourth row form a 10π aromatic system in $La_4B_{13}^-$ (2) matching the $4n + 2$ rule with n = 2, rendering an overall π-aromaticity to the system. The remaining 2 9c-2e $B_7(\pi)$–$La_2(d_\delta)$ bonds on the left and right ends of the fourth row with ON = 1.75 |e| and the totally delocalized 17c-2e bond over the whole molecule with ON = 2.00 |e| in the fifth row help to further stabilize the system. Thus, the high stability of $La_4B_{13}^-$ (2) originates from the unique (d–p)σ, (d–p)π, and (d–p)δ coordination bonds between the four La atoms and the chiral C_2 B_{13} framework consisting of two conjoined B_7 rings.

As indicated in Fig. 2b, $La_4B_{15}^-$ (4) possesses a similar bonding pattern with $La_4B_{13}^-$ (2). It has 12 2c-2e B–B periphery σ bonds on the axially chiral B_{15} ligand and 2 equivalent 3c-2e σ bonds over the two vertex-sharing B_3 triangles at center in the first row in an overall symmetry of D_2. There exist 3 10c-2e $B_8(\sigma)$–$La_2(d_{\pi/\sigma})$ bonds on the La_2B_8 inverse sandwich on the left and 3 10c-2e $B_8(\sigma)$–$La_2(d_{\pi/\sigma})$ bonds symmetrically distributed

on the right, forming two equivalent locally σ aromatic systems matching the $4n + 2$ rule ($n = 1$) in $La_4B_{13}^-$ (**2**). Meanwhile, the 5c-2e π bond in the third row and four 10c-2e $B_8(\pi)$–$La_2(d_{\pi/\sigma})$ bonds in the fourth row at the center form a 10π aromatic system following the $4n + 2$ rule ($n = 2$). Different from $La_4B_{13}^-$ (**2**), $La_4B_{15}^-$ (**4**) with a sepcial electronic count possesses 2 10c-2e $B_8(\pi)$–$La_2(d_\delta)$ bonds over the La_2B_8 inverse sandwich on the left and 2 10c-2e $B_8(\pi)$–$La_2(d_\delta)$ bonds symmetrically distributed over the La_2B_8 inverse sandwich on the right in the fourth row. Again, it is the σ + π dual aromaticity and unique (d–p)δ bonds between the four La atoms and the chiral D_2 B_{15} framework with two conjoined B_8 rings that render high stability to $La_4B_{15}^-$ (**4**).

The high-symmetry crown-like C_{3v} La_4B_{18} (**5**) appears to have an even more interesting bonding pattern (Fig. 2c). It possesses 12 isolated 2c-2e σ bonds on the B_{18} framemork and 4 isolated 3c-2e σ bonds on four B_3 triangles on the surface in the first row in an overall symmetry of C_{3v}. The following 15 10c-2e bonds in the second, third, and fourth rows are evenly distributed on three equivalent conjoined La_2B_8 inverse sandwiches embedded in the crown-shaped structure, including 3 10c-2e $B_8(\sigma)$–$La_2(d_{\sigma/\pi})$ bonds, 1 10c-2e $B_8(\sigma)$–$La_2(d_\pi)$ bond, and 1 10c-2e $B_8(\pi)$–$La_2(d_\delta)$ bond on each of the three conjoined La_2B_8 (**3**) inverse sandwiches, rendering local σ ($4n + 2 = 6$, $n = 1$) and π ($4n + 2 = 2$, $n = 0$) dual aromaticity to the system. The remaining 2 22c-2e bonds in the fifth row are delocalized over the whole neutral complex. Similar situations occur in Ac_4B_{18} (**5′**). The bonding patterns obtained above for $La_4B_{13}^-$ (**2**), $La_4B_{15}^-$ (**4**), and La_4B_{18} (**5**) are well in line with their corresponding canonical molecular orbitals (CMOs) depicted in Fig. S6 (ESI†).

The 3D aromatic nature of D_{7h} $La_2B_7^-$ (**1**), C_2 $La_4B_{13}^-$ (**2**), D_{8h} La_2B_8 (**3**), D_2 $La_4B_{15}^-$ (**4**), C_{3v} La_4B_{18} (**5**), D_{9h} $La_2B_9^-$ (**7**), and C_1 $La_5B_{24}^+$ (**9**) is further evidenced by their calculated nucleus-independent chemical shift (NICS) values. Based on the calculated NICS-ZZ components, Fig. 3 depicts their iso-chemical shielding surfaces (ICSS) with the Z-axis parallel to the designated C_7, C_2, C_8, C_2, C_3, C_9, or C_1 molecular axes to illuminate the chemical shieldings in these complexes, compared with that of benzene D_{6h} C_6H_6. Obviously, the space inside the complexes or within about 1.0 Å above the metal atoms in vertical direction belong to chemical shielding regions with negative NICS-ZZ values (highlighted in yellow), while the chemical de-shielding areas with positive NICS values (highlighted in green) are located outside the B_n ligands in horizontal direction. The ICSSs of these complexes appear to be similar to that of the prototypical aromatic benzene C_6H_6.[33]

1D, 2D, and 3D actinide boride nanomaterials

The highly stable cubic O_h $Ac_7B_{24}^+$ (**6′**) and O_h Ac_7B_{24} as embryos can be extended in x, y, and z three directions to form periodic actinide boride nanomaterials 1D $Ac_{10}B_{32}$ (**11′**) ($P4/mmm$), 2D Ac_3B_{10} (**12′**) ($P4/mmm$), and 3D AcB_6 (**13′**) ($Pm3m$) with the optimized lattice parameters of $a = 8.70$ Å, $a = b = 4.17$ Å, and $a = b = c = 4.22$ Å at PBE, respectively. These results are well comparable with the corresponding values of $a = 8.66$ Å,
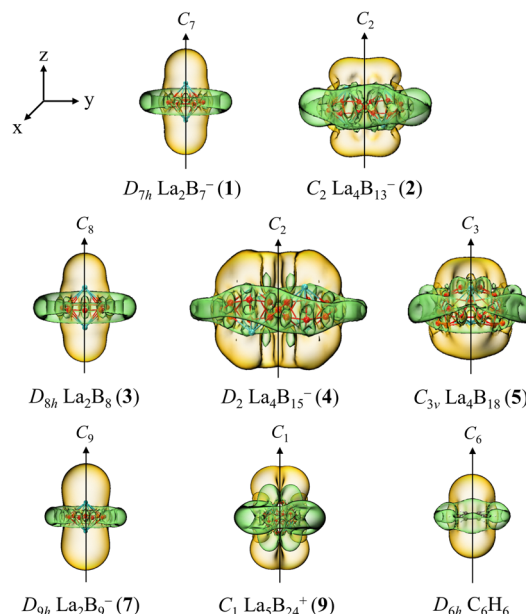

Fig. 3 Calculated iso-chemical shielding surfaces (ICSSs) of $La_2B_7^-$ (**1**), $La_4B_{13}^-$ (**2**), La_2B_8 (**3**), $La_4B_{15}^-$ (**4**), and La_4B_{18} (**5**), D_{9h} $La_2B_9^-$ (**7**), and C_1 $La_5B_{24}^+$ (**9**), in comparison with that of benzene D_{6h} C_6H_6. Yellow and green regions stand for chemical shielding and de-shielding areas, respectively.

$a = b = 4.17$ Å, and $a = b = c = 4.16$ Å calculated for their lanthanide boride counterparts 1D $La_{10}B_{32}$, 2D La_3B_{10}, and 3D LaB_6 at the same theoretical level.[32] The calculated La–B distances of $r_{Ac–B} = 3.10$ Å for 3D AcB_6 (**13′**), $r_{Ac–B(x)} = r_{Ac–B(y)} = 3.08$ Å, and $r_{Ac–B(z)} = 3.10$ Å for 2D Ac_3B_{10} (**12′**) also correspond well with the corresponding values in their lanthanide boride counterparts.[32] Similar Ac–B distances are obtained for 1D $Ac_{10}B_{32}$ (**11′**). It is worth noticing that cubic B_{24} frameworks with six conjoined B_8 rings in O_h $Ac_7B_{24}^+$ (**6′**) and O_h Ac_7B_{24} are well maintained in its 1D, 2D, and 3D nanostructures with infinite conjoined B_8 rings in periodical arrangements (Fig. 4).

Fig. 5 depicts calculated band structures and projected density of states (PDOS) of the most-concerned 2D Ac_3B_{10} (**12′**) and 3D AcB_6 (**13′**) which are expected to be synthesized in experiments. As expected, these nanostructures all appear to be metallic in nature, similar to their lanthanide counterparts. Both the B 2p orbitals and Ac 6d orbitals contribute to the calculated densities of states near the Fermi level. For 2D Ac_3B_{10} (**12′**), Ac–6d orbitals make major contributions to the PDOS above the Fermi level, while B-2p orbitals dominate the PDOS below it. However, for 3D AcB_6 (**13′**), B-2p orbitals dominate in both situations, with Ac 6d orbitals making minor contributions.

The calculated elastic constants of $C_{11} = 456$ Gpa, $C_{12} = 29$ Gpa, and $C_{44} = 114$ Gpa, Young's modulus of $Y = 340$ Gpa, and Poisson's ratio of $\nu = 0.17$ for 3D AcB_6 (**13′**) are well comparable with the corresponding measured[58]/calculated values of $C_{11} = 463/468$, $C_{22} = 45/23$, and $C_{44} = 89/91$ Gpa, $Y = 308/313$ Gpa, and $\nu = 0.22/0.19$ obtained for the experimentally known 3D LaB_6 (**13**). The results obtained above indicate that,
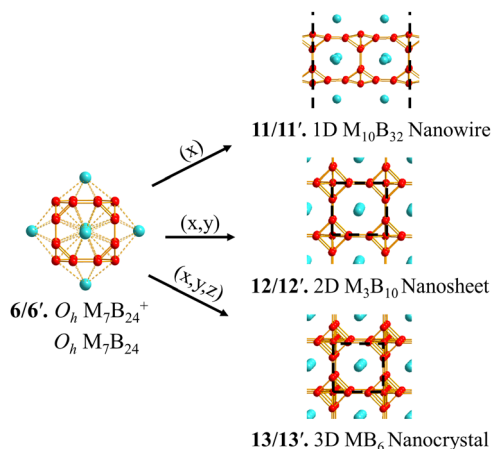
21082 | *Phys. Chem. Chem. Phys.*, 2022, **24**, 21078–21084

This journal is © the Owner Societies 2022

Fig. 4 Optimized structures of cubic O_h $M_7B_{24}{}^+$ (**6/6′**), O_h M_7B_{24}, 1D $M_{10}B_{32}$ nanowire (**11/11′**), 2D M_3B_{10} nanosheet (**12/12′**), and 3D MB_6 nanocrystal (**13/13′**) at PBE level (M = La, Ac).
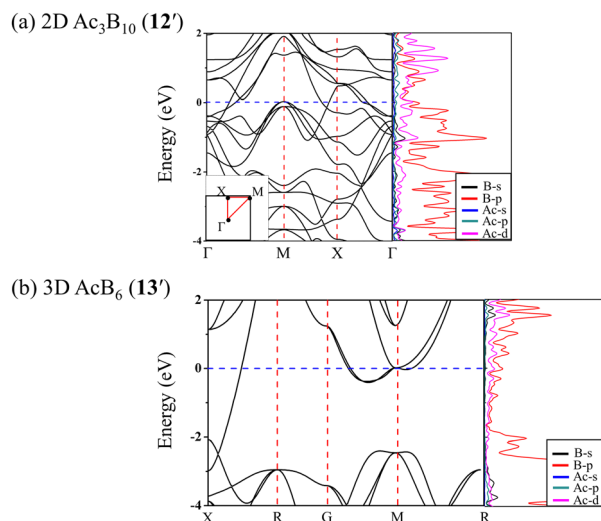

Fig. 5 Calculated band structures and projected densities of states (PDOS) of (a) 2D Ac_3B_{10} (**12′**) and (b) 3D AcB_6 (**13′**) at PBE level.

similar to their lanthanide boride counterparts, low-dimensional actinide boride materials 1D $Ac_{10}B_{32}$ (**11′**), 2D Ac_3B_{10} (**12′**), and 3D AcB_6 (**13′**) are expected to have excellent electronic, mechanical, and thermal properties, in particular, AcB_6 (**13′**) could be super-hard materials stable at high temperatures.

Conclusions

In summary, we have predicted in this work a series of novel lanthanide boride ($La_4B_{13}{}^-$ (**2**), $La_4B_{15}{}^-$ (**4**), $La_4B_{18}{}^-$ (**5**), and $La_5B_{24}{}^+$ (**9**)) and actinide boride ($Ac_2B_7{}^-$ (**1′**), $Ac_4B_{13}{}^-$ (**2′**), Ac_2B_8 (**3′**), $Ac_4B_{15}{}^-$ (**4′**), $Ac_4B_{18}{}^-$ (**5′**), $Ac_7B_{24}{}^+$ (**6′**), $Ac_2B_9{}^-$ (**7′**), Ac_4B_{24} (**8′**), $Ac_5B_{24}{}^+$ (**9′**), and $Ac_4B_{29}{}^-$ (**10′**)) nanoclusters based on boron frameworks composed of mono or conjoined B_n rings (n = 7–9). The newly proposed 1D $Ac_{10}B_{32}$ (**11′**) nanowire, 2D Ac_3B_{10} (**12′**) nanosheet, and 3D AcB_6 (**13′**) nanocrystal based on

periodic boron frameworks composed of infinite conjoined B_8 rings expand the previously reported low-dimensional lanthanide boride nanomaterials to their actinide boride counterparts, presenting viable possibility to synthesize actinide boride nanomaterials with novel properties in macroscopic quantities.

Conflicts of interest

There are no conflicts to declare.

Acknowledgements

Notes and references

1 F. A. Cotton, G. Wilkinson, C. A. Murillo and M. Bochmann, *Advanced inorganic chemistry*, Wiley, New York, 6th edn, 1999.

2 N. G. Szwacki, A. Sadrzadeh and B. I. Yakobson, *Phys. Rev. Lett.*, 2007, **98**, 166804.

3 X. Liu, Q. Li, Q. Ruan, M. S. Rahn, B. I. Yakobson and M. C. Hersam, *Nat. Mater.*, 2022, **21**, 35.

4 L. S. Wang, *Int. Rev. Phys. Chem.*, 2016, **35**, 69.

5 T. Jian, X. Chen, S. D. Li, A. I. Boldyrev, J. Li and L. S. Wang, *Chem. Soc. Rev.*, 2019, **48**, 3550.

6 Q. Chen, W. L. Li, Y. F. Zhao, S. Y. Zhang, H. S. Hu, H. Bai, H. R. Li, W. J. Tian, H. G. Lu, H. J. Zhai, S. D. Li, J. Li and L. S. Wang, *ACS Nano*, 2015, **9**, 754.

7 H. J. Zhai, Y. F. Zhao, W. L. Li, Q. Chen, H. Bai, H. S. Hu, Z. A. Piazza, W. J. Tian, H. G. Lu, Y. B. Wu, Y. W. Mu, G. F. Wei, Z. P. Liu, J. Li, S. D. Li and L. S. Wang, *Nat. Chem.*, 2014, **6**, 727.

8 H. Bai, T. T. Chen, Q. Chen, X. Y. Zhao, Y. Y. Zhang, W. J. Chen, W. L. Li, L. F. Cheung, B. Bai, J. Cavanagh, W. Huang, S. D. Li, J. Li and L. S. Wang, *Nanoscale*, 2019, **11**, 23286.

9 W. J. Chen, Y. Y. Ma, T. T. Chen, M. Z. Ao, D. F. Yuan, Q. Chen, X. X. Tian, Y. W. Mu, S. D. Li and L. S. Wang, *Nanoscale*, 2021, **13**, 3868.

10 E. Oger, N. R. Crawford, R. Kelting, P. Weis, M. M. Kappes and R. Ahlrichs, *Angew. Chem., Int. Ed.*, 2007, **46**, 8503.

11 Q. Q. Yan, T. Zhang, Y. Y. Ma, Q. Chen, Y. W. Mu and S. D. Li, *Nanoscale*, 2022, **14**, 11443.

12 D. L. Prasad and E. D. Jemmis, *Phys. Rev. Lett.*, 2008, **100**, 165504.

13 Q. Tong, L. Xue, J. Lv, Y. Wang and Y. Ma, *Faraday Discuss.*, 2018, **211**, 31.

14 F. Li, P. Jin, D. E. Jiang, L. Wang, S. B. Zhang, J. Zhao and Z. Chen, *J. Chem. Phys.*, 2012, **136**, 074302.

15 M. Zhang, H. G. Lu and S. D. Li, *Nano Res.*, 2021, **14**, 4719.

16 C. Romanescu, T. R. Galeev, W. L. Li, A. I. Boldyrev and L. S. Wang, *Angew. Chem., Int. Ed.*, 2011, **50**, 9334.

This journal is © the Owner Societies 2022

Phys. Chem. Chem. Phys., 2022, **24**, 21078–21084 | **21083**

17 T. R. Galeev, C. Romanescu, W. L. Li, L. S. Wang and A. I. Boldyrev, *Angew. Chem., Int. Ed.*, 2012, **51**, 2101.

18 I. A. Popov, W. L. Li, Z. A. Piazza, A. I. Boldyrev and L. S. Wang, *J. Phys. Chem. A*, 2014, **118**, 8098.

19 I. A. Popov, T. Jian, G. V. Lopez, A. I. Boldyrev and L. S. Wang, *Nat. Commun.*, 2015, **6**, 8654.

20 T. Jian, W. L. Li, I. A. Popov, G. V. Lopez, X. Chen, A. I. Boldyrev, J. Li and L. S. Wang, *J. Chem. Phys.*, 2016, **144**, 154310.

21 W. L. Li, T. Jian, X. Chen, H. R. Li, T. T. Chen, X. M. Luo, S. D. Li, J. Li and L. S. Wang, *Chem. Commun.*, 2017, **53**, 1587.

22 X. Q. Lu, H. G. Lu and S. D. Li, *RSC Adv.*, 2021, **11**, 27193.

23 W. L. Li, T. T. Chen, D. H. Xing, X. Chen, J. Li and L. S. Wang, *Proc. Natl. Acad. Sci. U. S. A.*, 2018, **115**, E6972.

24 T. T. Chen, W. L. Li, J. Li and L. S. Wang, *Chem. Sci.*, 2019, **10**, 2534.

25 W. L. Li, L. Xie, T. Jian, C. Romanescu, X. Huang and L. S. Wang, *Angew. Chem., Int. Ed.*, 2014, **53**, 1288.

26 Z. Y. Jiang, T. T. Chen, W. J. Chen, W. L. Li, J. Li and L. S. Wang, *J. Phys. Chem. A*, 2021, **125**, 2622.

27 T. T. Chen, W. L. Li, W. J. Chen, J. Li and L. S. Wang, *Chem. Commun.*, 2019, **55**, 7864.

28 T. T. Chen, W. L. Li, W. J. Chen, X. H. Yu, X. R. Dong, J. Li and L. S. Wang, *Nat. Commun.*, 2020, **11**, 2766.

29 X. Y. Zhao, M. Yan, Z. Wei and S. D. Li, *RSC Adv.*, 2020, **10**, 34225.

30 X. Q. Lu, Q. Chen, X. X. Tian, Y. W. Mu, H. G. Lu and S. D. Li, *Nanoscale*, 2019, **11**, 21311.

31 X. Q. Lu, C. Y. Gao, Z. Wei and S. D. Li, *J. Mol. Model.*, 2021, **27**, 130.

32 X. Q. Lu, M. Z. Ao, X. X. Tian, W. Y. Zan, Y. W. Mu and S. D. Li, *RSC Adv.*, 2020, **10**, 12469.

33 M. Z. Ao, X. Q. Lu, Y. W. Mu, W. Y. Zan and S. D. Li, *Phys. Chem. Chem. Phys.*, 2022, **24**, 3918.

34 X. Chen, Y. F. Zhao, Y. Y. Zhang and J. Li, *J. Comput. Chem.*, 2019, **40**, 1105.

35 C. Adamo and V. Barone, *J. Chem. Phys.*, 1999, **110**, 6158.

36 J. Tao, J. P. Perdew, V. N. Staroverov and G. E. Scuseria, *Phys. Rev. Lett.*, 2003, **91**, 146401.

37 R. Krishnan, J. S. Binkley, R. Seeger and J. A. Pople, *J. Chem. Phys.*, 1980, **72**, 650.

38 M. Dolg, H. Stoll and H. Preuss, *Theor. Chim. Acta*, 1993, **85**, 441.

39 M. Dolg, H. Stoll, A. Savin and H. Preuss, *Theor. Chim. Acta*, 1989, **75**, 173.

40 A. Moritz, X. Cao and M. Dolg, *Theor. Chem. Acc.*, 2006, **117**, 473.

41 M. J. Frisch, G. W. Trucks, H. B. Schlegel, *et al.*, *Gaussian 09, Revision D.01*, Gaussian Inc., Wallingford CT, 2013.

42 G. D. Purvis Iii and R. J. Bartlett, *J. Chem. Phys.*, 1982, **76**, 1910.

43 J. Čížek, *Adv. Chem. Phys.*, 1969, **14**, 35.

44 K. Raghavachari, G. W. Trucks, J. A. Pople and M. Head-Gordon, *Chem. Phys. Lett.*, 1989, **157**, 479.

45 H. J. Werner, P. J. Knowles, G. Knizia, F. R. Manby and M. Schütz, *Wiley Interdiscip. Rev.: Comput. Mol. Sci.*, 2012, **2**, 242.

46 G. Kresse and J. Furthmuller, *Phys. Rev. B: Condens. Matter Mater. Phys.*, 1996, **54**, 11169.

47 G. Kresse and J. Hafner, *J. Phys.: Condens. Matter*, 1994, **6**, 8245.

48 P. E. Blochl, *Phys. Rev. B: Condens. Matter Mater. Phys.*, 1994, **50**, 17953.

49 G. Kresse and D. Joubert, *Phys. Rev. B: Condens. Matter Mater. Phys.*, 1999, **59**, 1758.

50 J. P. Perdew, K. Burke and M. Ernzerhof, *Phys. Rev. Lett.*, 1996, **77**, 3865.

51 W. L. Li, C. Ertural, D. Bogdanovski, J. Li and R. Dronskowski, *Inorg. Chem.*, 2018, **57**, 12999.

52 V. I. Anisimov, I. V. Solovyev, M. A. Korotin, M. T. Czyzyk and G. A. Sawatzky, *Phys. Rev. B: Condens. Matter Mater. Phys.*, 1993, **48**, 16929.

53 N. V. Tkachenko and A. I. Boldyrev, *Phys. Chem. Chem. Phys.*, 2019, **21**, 9590.

54 P. E. D. Glendening, J. K. Badenhoop, A. E. Reed, J. E. Carpenter, J. A. Bohmann, C. M. Morales, C. R. Landis and F. Weinhold, *NBO 6.0*, 2013.

55 J. Vandevondele, M. Krack, F. Mohamed, M. Parrinello, T. Chassaing and J. Hutter, *Comput. Phys. Commun.*, 2005, **167**, 103.

56 E. Kleinpeter, S. Klod and A. Koch, *THEOCHEM*, 2007, **811**, 45.

57 T. Lu and F. Chen, *J. Comput. Chem.*, 2012, **33**, 580.

58 A. E. Baranovskiy, G. E. Grechnev, V. D. Fil, T. V. Ignatova, A. V. Logosha, A. S. Panfilov, I. V. Svechkarev, N. Y. Shitsevalova, V. B. Filippov and O. Eriksson, *J. Alloys Compd.*, 2007, **442**, 228.